1 **HR-GLDD: A globally distributed dataset using generalized DL for rapid landslide**
2 **mapping on HR satellite imagery**

3 Sansar Raj Meena [1], Lorenzo Nava [1], Kushanav Bhuyan [1], Silvia Puliero [1], Lucas Pedrosa
4 Soares [2], Helen Cristina Dias [2], Mario Floris [1], Filippo Catani [1*]

6   1. Machine Intelligence and Slope Stability Laboratory, Department of Geosciences,
7   University of Padova, 35129 Padua, Italy
8   2. Institute of Energy and Environment, University of São Paulo, São Paulo 05508-010,
9   Brazil

11 * Correspondence:sansarraj.meena@unipd.it

13 **Abstract:**
14 Multiple landslide events occur often across the world which have the potential to cause
15 significant harm to both human life and property. Although a substantial amount of
16 research has been conducted to address mapping of landslides using Earth Observation
17 (EO) data, several gaps and uncertainties remain when developing models to be
18 operational at the global scale. To address this issue, we present the HR-GLDD, a high
19 resolution (HR) dataset for landslide mapping composed of landslide instances from ten
20 different physiographical regions globally: South and South-East Asia, East Asia, South
21 America, and Central America. The dataset contains five rainfall triggered and five
22 earthquake-triggered multiple landslide events that occurred in varying geomorphological
23 and topographical regions. HR-GLDD is one of the first dataset for landslide detection
24 generated by high resolution satellite imagery which can be useful for applications in
25 artificial intelligence for landslide segmentation and detection studies. Five state of the art
26 deep learning models were used to test the transferability and robustness of the HR-
27 GLDD. Moreover, two recent landslide events were used for testing the performance and
28 usability of the dataset to comment on the detection of newly occurring significant landslide
29 events. The deep learning models showed similar results for testing the HR-GLDD in
30 individual test sites thereby indicating the robustness of the dataset for such purposes.
31 The HR-GLDD can be accessed open access and it has the potential to calibrate and
32 develop models to produce reliable inventories using high resolution satellite imagery after
33 the occurrence of new significant landslide events. The HR-GLDD will be updated regularly
34 by integrating data from new landslide events.

35

36   1. Introduction

37 With the increasing impacts of climate change, increased urbanization, and anthropogenic
38 pressure in recent years, the risk from hazards to population, infrastructure, and essential life
39 services has exacerbated. Landslides are quite ubiquitous and account for approximately
40 4.9% of all the natural disasters and 1.3% of the fatalities in the world (EM-DAT, 2018).
41 Induced by natural (earthquakes, volcanic eruptions, meteorological events) and
42 anthropogenic triggers (slope modifications, mining, landscape engineering), the increase in
43 the stress of slope materials causes landslides, which can harm numerous elements at risk.
44 Landslides occur heterogeneously in many parts of the world including the Central and South
45 Americas, the Caribbean islands, Asia, Turkey, European Alps, and East Africa (Froude &
46 Petley, 2018). In the past 15 years, we have seen a high number of events that have
47 inadvertently led to the failure of thousands of slopes and causing damage to essential linear
48 infrastructures and population. Some recent examples are Wenchuan, China (2008),

49   Kedarnath, India (2013), Kaikoura, New Zealand (2016), Jiuzhaigou, China (2017), Dominica
50   (2017), Porgera, Papua New Guinea (2018), Hokkaido, Japan (2018), Belluno, Italy (2018),
51   Haiti (2021), Sumatra, Indonesia (2022).

52   These examples indicate that landslide occurrences will probably continue to increase in the
53   short and medium term; therefore, an effective capability of rapid mapping is required to map
54   future event-based landslides and reduce expecetd losses. In recent years, state-of-the-art
55   research has been conducted to better understand the impact of natural hazards such as
56   landslides and the cascading effects on the elements-at-risk. A critical understanding of these
57   complex processes begins with the onset of mapping slope failures. This information about
58   the failed slopes is attributed as records and is documented in a "landslide inventory".
59   Landslide inventories include information on the spatial location and extent of the landslides
60   and, if available, also crucial information about 1) the time of occurrence, 2) the triggering
61   event that led slopes to fail, 3) the typology of the landslides based on the accepted standard
62   classifications like (Cruden & Varnes, 1996) and (Hungr et al., 2014), and 4) the volume of the
63   failure. However, regarding rapid mapping of recently occurred landslides, information about
64   the spatial location, distribution, and intersection with affected elements-at-risk are important.

65   When it comes to detecting and mapping landslides over remotely sensed images, it is safe
66   to say that a lot of the current literature in the past couple of years has devised and spent time
67   employing artificial intelligence (AI) models to map landslides automatically, arguably, with
68   good results. These AI models can classify remote sensing images to denote where the
69   landslides are present in the analysed images. However, the core prerequisite for employing
70   AI models is a reliable dataset to be used for training. Recent studies have only focused on
71   mapping landslides with AI but at scales that are small or regional while also claiming that the
72   proposed models can cater towards rapid mapping of landslides at any given time, location
73   and scale (Liu et al., 2022; Meena et al., 2022a; Nava, Bhuyan, et al., 2022; Nava, Monserrat,
74   et al., 2022; Soares et al., 2022a; Tang et al., 2022; Yang et al., 2022; Yang & Xu, 2022).
75   However, seldom has been the case where truly an approach has been taken to map
76   landslides outside the regions where the models are initially trained on, and also towards
77   actually applying the proposed models in capturing and mapping event-based landslides that
78   has recently occurred. Some recent works at collectively detecting and mapping landslides of
79   different countries have been attempted by (Prakash et al., 2021) and (Ghorbanzadeh et al.,
80   2022), which showcases the power of employing AI at mapping landslides. However, the core
81   of these studies also heavily relies on the availability of quantity and quality data for training
82   an AI model. The accessibility of such data can 1) allow a model to identify landslides that
83   were caused by different types of triggers (logically leading to the detection of different types
84   of landslides), 2) to map landslides in different parts of the world that vary geomorphologically,
85   and 3) the applicability of the model at mapping newly occurring landslides triggered by events
86   in recent times. The contemporary works of the current literature brings about a critical
87   discussion about the availability and accessibility of comprehensive and adequate data to
88   effectively train models to detect landslides. Both (Prakash et al., 2021) and (Ghorbanzadeh
89   et al., 2022) have used open-source Sentinel-2 imageries for multi-site landslide detection
90   however, considering the fact that the spatial resolution is 10 metres, a lot of small landslides
91   are missed out or not accurately captured (Meena et al., 2022b). The latter attempted to design
92   a benchmark data set for landslide model training using moderate resolution sentinel-2 data
93   and combined it with DEM derived data from ALOS-PALSAR. However, they only considered
94   four study areas while training the model on 25% of area and testing the model performances
95   in the remaining 75% area. Furthermore, they had varying non-uniform results for each of the
96   models trained on the dataset. This showcases that a quality dataset is still not available where
97   different models can give consistent results across the board.

98   To effectively and rapidly map landslides after an event, it is required first to determine the
99   spatial extent of the affected areas. Collecting this data is frequently hazardous since it
100 involves individuals on the ground investigating landslides first hand during or immediately
101 after the event. With the increased availability of satellite imagery, this task has the potential
102 to be completed not only remotely but also automatically through the use of powerful deep
103 learning algorithms. Currently, adequate high-resolution satellite imagery of landslides is not
104 widely available. To depict the complex and dynamic nature of the landslides, significant
105 amounts of images must be provided. To that purpose, we present High resolution Global
106 landslide dataset (HR-GLDD), a large-scale satellite image dataset with produced landslide
107 inventories.

108

109 2. Study areas

110 The study areas were chosen based on the variety of triggering events that resulted in the
111 occurrence of the landslides. Because of the availability of VHR archived Planet Scope
112 imageries after 2016, the most significant landslide events were considered. The
113 geomorphological diversity of the study sites results in a collection of complex landslide
114 phenomenon. We selected the imageries based on the availability of cloud-free conditions in
115 the areas and examined globally archived satellite remote sensing imageries from Planet
116 Scope from the years between 2017 and 2022 (Table 1). We selected 8 study sites across the
117 globe to assemble the database (see figure1). To further test the generalization capabilities of
118 the models trained on the proposed dataset, we choose two recently occurred events: co-
119 seismic landslides in Haiti (August, 2021) and rainfall-induced landslides in Indonesia
120 (February, 2022).
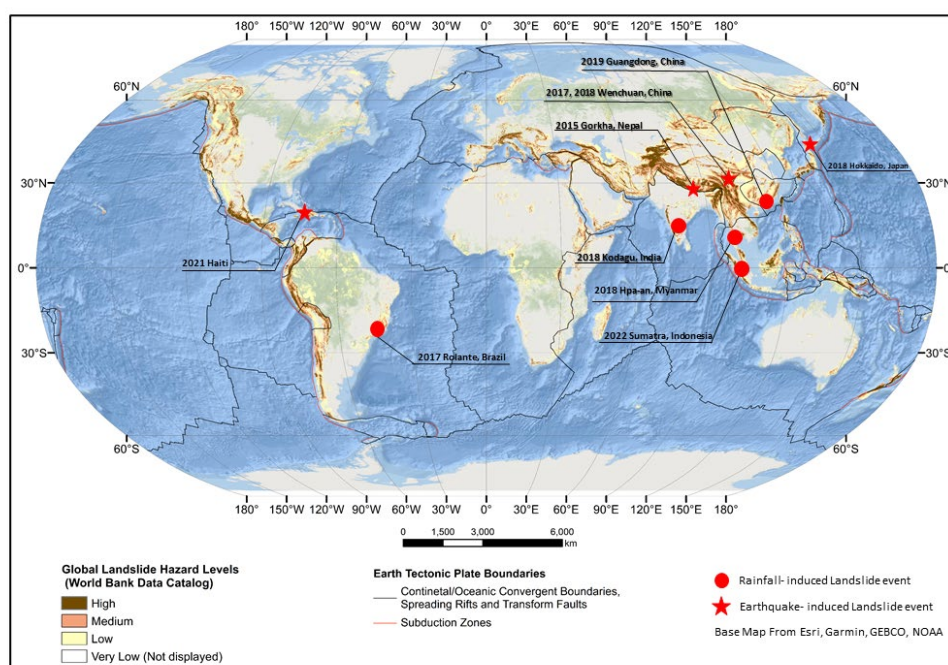
121

122 Figure 1: Rainfall and earthquake induced landslide events present in the HR-GLDD.

2.1. Study areas

2.1.1. Papua New Guinea

Papua New Guinea (PNG) is located on the Australian continent and is the eastern half sector of the New Guinea island. The region is characterized by active volcanos, earthquakes, elevations up to ~4.400 m.a.s.l., steep slopes and is part of the 'Ring of Fire' in the Pacific Ocean. Regarding the tectonic and geological elements, the island can be divided into four tectonic belts: Stable platform, Fold Belt, Mobile Belt, and Papuan Fold and Thrust Belt (Tanyaş et al. 2022). The east sector, where PNG is located has the presence of accreted Paleozoic structure of Tasman Orogen (Hill and Hall, 2003). Due to these conditions, the area is frequently affected by landslides associated with the occurrence of earthquakes (Tanyaş et al. 2022). On February 25, 2018, in the southern area of the Papuan Fold and Thrust belt (central highlands of PNG), a severe earthquake occurred, the magnitude hit Mw 7.5. The event was responsible for damage to buildings, and energy structures besides triggering a high number of landslides (Wang et al. 2020). Around 11,600 landslide scars were registered, and more than half had 50,000 m² (Tanyaş et al. 2022), according to Wang et al. 2020, the earthquake hit the highest magnitude in the region in the past 100 years.

2.1.2. Kodagu, India

Kodagu district is located in the Karnataka state, Western Ghats, India. The area is characterized by elevations approximately between 50 and 1.750 m a.s.l., metamorphic rocks (e.g., amphibolite, gneiss, and schist), steep slopes, high annual precipitation of about 4000 mm, and the presence of croplands (e.g., coffee, rice, and spices) (Jennifer and Saravan, 2020; Meena et al. 2021). In August 2018, a rainfall-induced high magnitude mass movement event occurred in Kodagu, the primary landslide type triggered was debris flow (Meena et al. 2021). A total of 343 landslides were recorded, including mudflows, rock falls, and debris flows (Meena et al. 2021). The event resulted in several damages to land resources, properties, and loss of human lives (Martha et al. 2018; Jennifer and Saravan, 2020).

2.1.3. Rolante, Brazil

The Rolante river catchment study area is located in the Rio Grande do Sul state, southern Brazil. The region being part of the Serra Geral geomorphological unit, has elevations up to ~1.000 m.a.s.l. (Uehara et al. 2020). Moreover, is characterized by the presence of basaltic rocks and sandstones, and annual precipitation thresholds between 1700 and 2000 mm (Uehara et al. 2020, Soares et al. 2022). On 5 January 2017, a high magnitude rainfall-induced mass movement event was triggered, and 308 landslides were registered (Gameiro et al. 2019; Quevedo et al. 2019), resulting in several damages to the Rolante municipality.

2.1.4. Tiburon Peninsula, Haiti

The Tiburon Peninsula study area is located in the western part of the Hispaniola island (Haiti) with elevation up to 2300 m. a.s.l. Tiburon Peninsula, mainly consists of volcanic rocks such as basalts and sedimentary rocks, namely limestones (Harp et al., 2016). The annual precipitation of the area is more than 1600 mm (Alpert, 1942; USAID, 2014). On 14 August 2021, Tiburon Peninsula was struck by a Mw 7.2 earthquake, which was followed by several aftershocks. The strongest one (Mw 5.7) occurred on 15 August 2021. Two days after the mainshock the area was hit by the intense Tropical Cyclone Grace. The combination of the

167 two events triggered thousands of landslides (Martinez et al., 2021) in the Pic Macaya National
168 Park located in western part of the peninsula.

169   2.1.5. Rasuwa, Nepal

170 The study area is located in the Rasuwa district (central Nepal) in the higher Himalayas with
171 altitudes ranging from 904 to 3267 m. a.s.l and annual average precipitation of 1800-2000 mm
172 (Karki et al., 2016),The geology includes Proterozoic metamorphic rocks such as amphibolite,
173 gneiss, and schist (Tiwari et al., 2017). The area was struck by the Mw 7.8 Gorkha earthquake
174 on 25 April 2015. The intense seismic sequence produced at least 25,000 landslides (Roback
175 et al., 2018).

176   2.1.6. Hokkaido, Japan

177 The Hokkaido study area is in northern Japan and has a high presence of croplands. The area
178 is characterized by elevations between 50 and 500 m a.s.l., the geology is composed of
179 Neogene sedimentary rocks, formed by the accumulation of numerous layers formed by
180 materials ejected by the Tarumai volcano from several events over the years (Yamagishi and
181 Yamazaki, 2018; Zhao et al. 2020; Koi et al. 2022). A severe earthquake hit the Hokkaido
182 Iburi-Tobu area in Japan on September 6th, 2018. The earthquake registered a magnitude of
183 6.7 according to the Japan Meteorological Agency (JMA) and its epicenter was at 42.72° North
184 and 142.0° East (Yamagishi and Yamazaki, 2018), located along the southern frontier of
185 Hokkaido. The event triggered thousands of landslides (~7059) in a concentrated area of 466
186 km² (Zhao et al. 2020) and was responsible for 36 deaths (Yamagishi and Yamazaki, 2018).

187   2.1.7. Wenchuan, China

188 The study area is in the Longmenshan region at the eastern margin of the Tibetan Plateau,
189 China. The location is characterized by high elevations up to 7.500 m a.s.l., the geology
190 consists of lithological units from the Mesozoic, Jurassic, Cretaceous, Paleozoic, Precambrian
191 formations and three types of Quaternary sedimentary units (Qi et al. 2010; Gorum et al.
192 2011). The area is constantly affected by earthquake-induced landslides over the years (e.g.,
193 2017, 2018, 2019, 2021). The 2008 Wenchuan event is one of the most destructive events of
194 mass movements related to earthquakes in the region (Fan et al. 2018). The Wenchuan
195 earthquake hit a magnitude of Mw 7.9. It was responsible for triggering nearly 200.000
196 landslides (Xu et al. 2014), besides missing, injured, and thousands of human fatalities in a
197 total area of 31,686.12 km² (Qi et al. 2010).

198

199   2.1.8. Sumatra, Indonesia

200 The investigated area is Mount Talamau (2912 m) which is a compound volcano located in
201 West Pasaman Regency, West Sumatra Province, Indonesia. Geologically, the volcano
202 consists of andesite and basalt rocks belonging to Pleistocene-Holocene age (Fadhilah &
203 Prabowo, 2020; Zulkarnain, 2016). The climate of the area is humid and tropical and the mean
204 annual precipitation in West Pasaman area is between 3500 and 4500 mm/year (Wilis, 2019).
205 The Mw 6.1 earthquake hit West Sumatra on 25 February 2022. This event triggered several
206 landslides in an area of 6 km², along the eastern and north-eastern flank of Talamau volcano.

207   2.1.9. Longchuan, China

208 The study area is located in the vicinity of Mibei village in Longchuan County, Guangdong
209 Province, China with elevations between 180 and 600 m. The area has a subtropical monsoon
210 climate, affected by frequent typhoons and rainstorms from May to October. The average

211 annual precipitation ranges from 1300 to 2500 mm (Bai et al., 2021). The area is composed
212 of Paleozoic completely weathered granite and Quaternary granite residual soil (Bai et al.,
213 2021). Between 10 and 13 June 2019, an intense rainfall event, which was characterized by
214 cumulative rainfall of 270 mm, triggered 327 shallow landslides between 300 and 400 m of
215 altitudes and slopes ranging from 35 to 45° (Feng et al., 2022).

216 ### 2.1.10. Hpa-An, Myanmar

217 The study area is located in Hpa-An district (central Kayin State, South Myanmar) in a tropical
218 and monsoon area with a mean annual precipitation between 4500 and 5000 mm (Win Zin &
219 Rutten, 2017) and elevations up to 1300 meters. The area is part of the Shan Plateau
220 sequence, which includes low grade metamorphosed Precambian, Palezoic and Mesozoic
221 sedimentary rocks (Jain & Banerjee, 2020). On 28–30 July 2018, Myanmar was hit by an
222 extreme rainfall event which caused a flood along Bago river basin and triggered 992
223 landslides only in Kayin State (Amatya et al., 2022).

224 ## 3. Data set description

225 The dataset created in this study consists of images acquired from the PlanetScope satellites
226 (see table 1) and landslide inventories collected from the literature. For some events,
227 landslides were manually delineated due to unavailability of existing inventories. PlanetScope
228 is a constellation of approximately 130 satellites that acquire images of the Earth daily with 3
229 meters of spatial resolution. The sensors acquire the images with 8 spectral bands: coastal
230 blue (431 - 552 nm), blue (465 - 515 nm), green (547 - 583 nm), yellow (600 - 620 nm), red
231 (650 - 680 nm), red-edge (697 - 713 nm) and NIR (845 - 885 nm) (Planet Team, 2019)(Planet
232 Team, 2019)(Planet Team, 2019)(Planet Team, 2019)(Planet Team, 2019)(Planet Team,
233 2019)(Planet Team, 2019)(Planet Team, 2019)(Planet Team, 2019). PlanetScope imagery
234 consists of surface reflectance values and 16 bits images. The images from both sensors are
235 orthorectified and radiometrically corrected by the providers.

236 The dataset was prepared using only the red, green, blue, and NIR bands. The pre-processing
237 phase was based on three steps: generation of binary masks, data sampling, and tiles
238 patching. First, the interpreted landslides polygons from each area were rasterized using the
239 Rasterio Python library into a binary mask, where "1" represents the landslides and "0" the
240 background. The satellite imagery, along with the mask was then sampled and patched into a
241 regular grid that yields patches of dimension 128 x 128 pixels, which correspond to 14.7 km^2
242 per patch. Since the imbalance between background area and landslides is strong, the images
243 that did not have any landslides pixel labelled were removed. Table 1 shows the number of
244 tiles created for each area.
245
246 Table 1 - Number of tiles, satellite information and landslide statistics for each study area.

Study Area	Satellite	Number of tiles	Study Area in km^2	Number of landslides	Minimum Landslide area (m^2)	Maximum Landslide area (m^2)	Total Landslide area (km^2)	Source
Kodagu (India) 2018	PlanetScope	530	4033.62	343	276.23	581342.19	5.67	(Meena et al., 2021a)
Rolante (Brazil) 2017	PlanetScope	33	24.62	113	381.76	81277.53	0.67	(Soares et al., 2022b)

Tiburon Peninsula, (Haiti) 2021	PlanetScope	461	130.85	1394	200.74	473696	8.24	This Study
Rasuwa (Nepal) 2017	PlanetScope	222	114.68	184	676.85	115567.96	2.45	(Meena et al., 2022e)
Hokkaido (Japan) 2018	PlanetScope	159	50.17	715	237.76	48524.72	5.29	(Wang et al., 2019)
Wenchuan (China) 2017	PlanetScope	284	58.25	1415	23.78	98467.96	3.19	(Fan et al., 2019)
Wenchuan (China) 2018	PlanetScope	263	58.25	546	110.18	1289210.19	5.54	This study
Sumatra, (Indonesia) 2022	PlanetScope	403	22.56	584	302.26	6206089.32	9.73	This study
Longchuan, (China) 2019	PlanetScope	116	32.22	228	235.21	61163.17	0.73	This study
Hpa-An, (Myanmar) 2018	PlanetScope	108	28.38	540	101.23	88044.20	0.97	This study

247

248

3.1. High-Resolution Global Landslide Detector Database (HR-GLDD) design

The performance evaluation of the study sites was carried out using metrics and trained using five state-of-the-art U-net like models, showcasing the capability and applicability of the High Resolution Global Landslide Detector Database (HR-GLDD). We used a total of ten geographically distinct study sites distributed globally, where landslide events were chosen including different triggering mechanisms such as five earthquakes induced and five rainfall induced landslide affected sites. We generated image patches for the first 8 sites of Table 1. For each area we separately divide the patches into 60% for training, 20% for validation, and 20% for testing the model capabilities. All the sets are then mixed to create a unique dataset composed by equal percentages of patches.

We designed three scenarios to train, predict, and evaluate model performances in order to assess the robustness and applicability of the HR-GLDD. Primarily, we evaluate the model performances on the individual test sets. Secondly, we evaluate the performances of the models on the HR-GLDD test set. Moreover, finally, we test on two completely unseen recently occurred landslide events in Haiti 2021 and Indonesia 2022 (see figure 2).
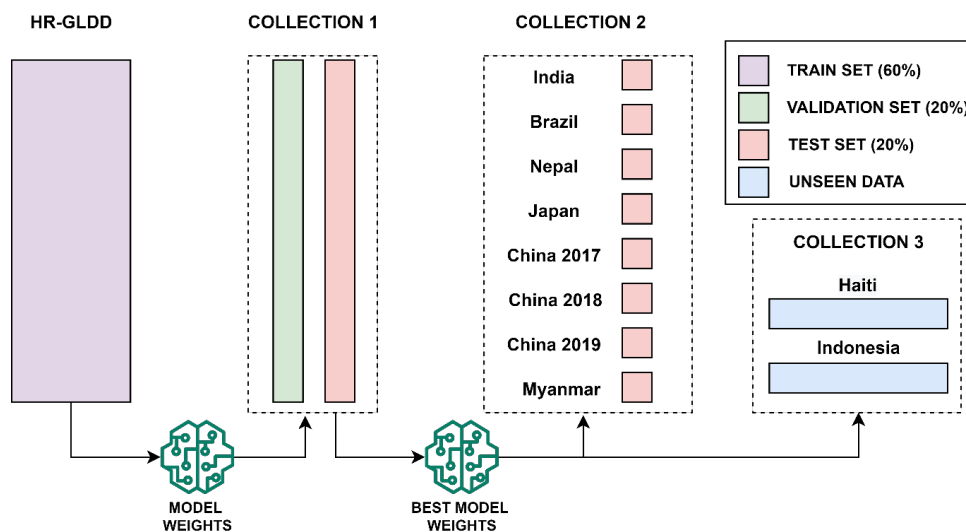
264

265 Figure 2: Schematic representation of the division of different components of HR-GLDD.
266 Collection 1 refers to the test data separated from the HR-GLDD. Collection 2 refers to the
267 test dataset of individual sites. Collection 3 refers to two recent data set for testing purposes.

268

269 4. Methodology

270

271 4.1. Model Architectures

272 The proposed dataset is evaluated through several state-of-the-art Deep Learning
273 segmentation models. In the past years, the U-Net (Abderrahim et al., 2020) has been used
274 in several landslide detection applications which yield generally the most reliable results
275 (Bhuyan et al., 2022; Meena et al., 2022c; Nava, Bhuyan, et al., 2022). Therefore, we decide
276 to use it as a benchmark model when training on the proposed dataset. Moreover, several
277 improved versions of the same are evaluated. We systematically trained the model using a
278 variety of combinations of the hyper-parameters batch size (8, 16, 32, 64), learning rate (5e-
279 4, 10e-4, 5e-5, 10e-5) and the number of filters (8, 16, 32, 64). A description of the employed
280 architectures is given in this section.

281

282   4.1.1. U-Net

283

284 U-Net has been utilized in various semantic segmentation applications, yielding generally
285 outstanding results (Abderrahim et al., 2020). U-Net was employed initially in biomedical
286 picture segmentation (Ronneberger et al., 2015). Low-level representations are captured by a
287 contracting path (encoder), whereas a decoding path captures high-level representations. The
288 encoding path consists of successive convolution blocks and is equivalent to a traditional CNN
289 structure. Two convolutional layers with a 3 x 3 kernel size and a 2 x 2 max-pooling layer are
290 present within every convolutional block. The rectified linear unit (ReLU) activation function is
291 used to activate each convolutional layer (Fred Agarap, n.d.). A 2 x 2 max-pooling layer is
292 added to the convolutional block's end in the encoder route to conduct non-linear
293 downsampling, whereas, in the decoder path, a 2 x 2 upsampling layer takes its place. The
294 upsampling layer is positioned right after a 3x3 convolutional layer (see figure 3). We refer to
295 this combination as learnable upconvolution.

296
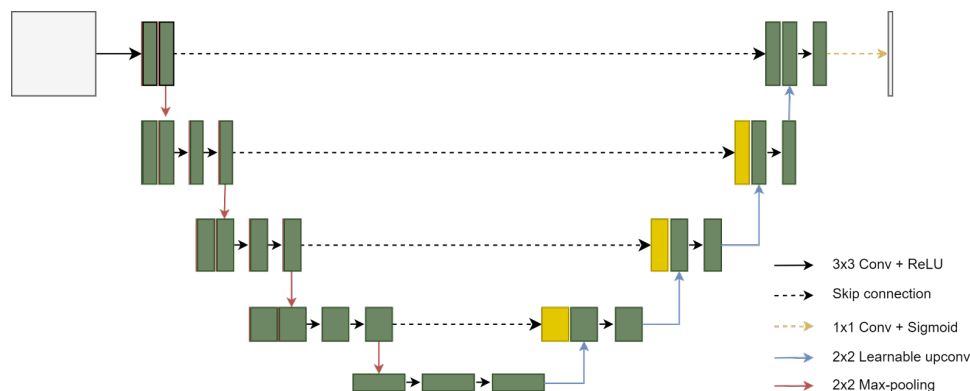
297
298
299   Figure 3: Model architecture of U-Net.

300
301   4.1.2.   Residual U-Net (Res U-Net)

302
303   Res U-Net (Diakogiannis et al., 2020) follows the same U shape as U-Net, whereas here the
304   above-explained convolutional blocks are replaced by residual blocks. This architecture's goal
305   is to improve the learning capacities of the conventional U-Net as well as mitigate the gradient
306   vanishing effect, especially when dealing with deep neural networks (such as U-Net) (see
307   figure 4).

308
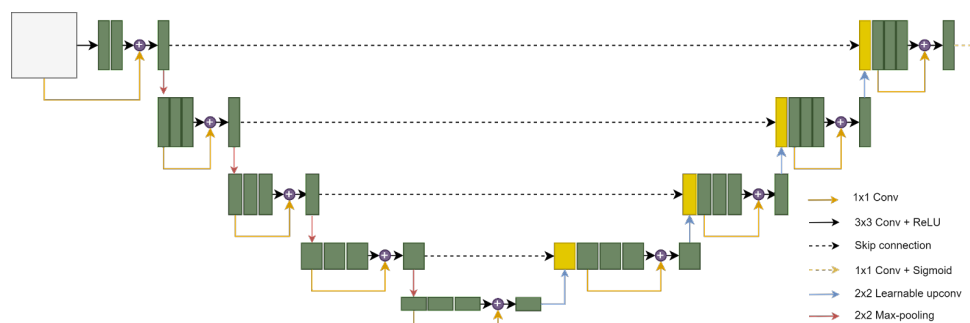
309
310
311   Figure 4: Model architecture of the Res U-Net.

312
313
314   4.1.3.   Attention U-Net and Attention Res U-Net

315
316   In the conventional U-Net as well as in the Res U-Net, cascading convolutions have been
317   shown to provide false alerts for tiny objects with high form variability (Oktay et al., n.d.). To
318   select pertinent spatial information from low-level maps and therefore alleviate the problem,
319   soft attention gates (AGs) are added (see figure 5). The attention gates are built on skip
320   connections, which actively inhibit activations in unnecessary areas, lowering the number of
321   duplicated features (Abraham & Mefraz Khan, 2018).

322
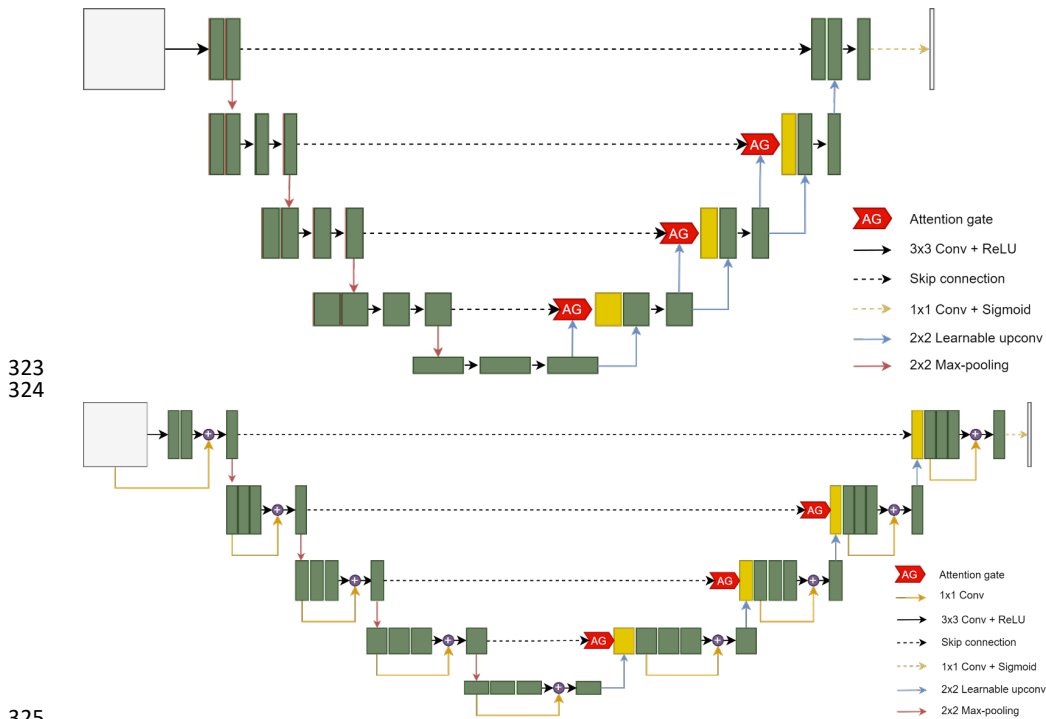
323
324

325
326
327   Figure 5: Model architecture of the (a) Attention U-Net and (b) Attention Res U-Net.
328
329
330   4.1.4. Attention Deep Supervision Multi-Scale (ADSMS) U-Net
331   This architecture adopts the Attention U-Net structure, while, in addition, multi-scale image
332   pyramid inputs are fed to the model, and a deep supervision strategy is applied (Abraham &
333   Mefraz Khan, 2018). In practice, multi-scale inputs enable the model to gather that class data,
334   which is more readily available at various sizes. This holds true for both background features
335   and landslides. Lastly, where training data are few and networks are relatively shallow, deep
336   supervision conducts a potent "regularization". More details about the deep supervision
337   strategy used are available in the following section (see figure 6).
338
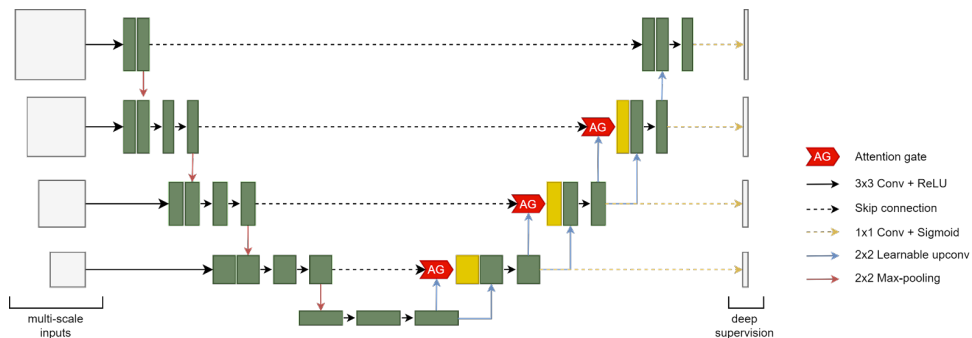
339
340
341   Figure 6: Model architecture of the Attention Deep Supervision Multi-Scale U-Net.
342

4.2. Models training

To train the DL models, we utilized Dice Loss (Milletari et al., n.d.) as the loss function:

$$\text{Dice Loss} = c\frac{1}{N}\sum_{i=1}^{} p_i c g_i c + \sum_{i=1}^{N} p_i c + g_i c$$

Equation (1) illustrates a two-class Dice score coefficient (DSC) variation for class c, where $g_i c$ [0, 1] and $p_i c$ [0, 1] are the ground truth and predicted labels, respectively. Furthermore, the numerical stability is assured by avoiding division by zero, while N specifies the total number of picture pixels. As an exception, in the ADSMS U-Net model, every high-dimensional feature representation is regulated by Focal Tversky Loss to avoid loss over-suppression, while the final output is controlled by the conventional Tversky Loss. This deep supervision strategy, described in (Lee et al., n.d.), requires intermediate layers to be semantically discriminative at all scales. Furthermore, it contributes to ensuring that the attention unit has the power to change responses to a wide variety of visual foreground material. This strategy is adopted from (Abraham & Mefraz Khan, 2018), who propose it along with the ADSMS U-Net architecture. As the loss function optimizer, for all the models, we used a stochastic gradient descent strategy based on an adaptive estimate of first- and second-order moments (Adam), which is useful in problems with uncertain data and sparse gradients (Kingma & Lei Ba, n.d.). The precision, recall, F1-score, and Intersection Over Union (IOU) score, the most common accuracy evaluation measures for segmentation models, all of which have been utilized in several landslide detection studies, were used to measure how well the applied DL models performed in detecting landslides. The appropriate combinations of hyper-parameters must be used while training such DL models in order to optimize the model and, therefore, output the best results.

5. Results

5.1. HR-GLDD evaluation results

The robustness and applicability of the HR-GLDD was tested using the best model weight. We train and calibrate the models using the HR-GLDD. The best weighs for each model are selected based on the model performances on the mixed test set of the HR-GLDD dataset. After running the models on test dataset, batch size of 4 and Adam optimiser with learning rate 1e-3 resulted in best model weight. To further evaluate the efficiency and generalization capabilities of the models, we use the model on two unseen datasets to map landslides in the two different geomorphological areas that were recently affected by multiple landslide events. We chose the most recent events one occurred after Haiti earthquake in August 2021 and another one in Sumatra, Indonesia after a heavy rainfall event of February 2022. A total of 461 and 403 unseen image patches were evaluated for Haiti and Indonesia, respectively.

Experimental results for landslide detection by utilising the HR-GLDD are presented in Table 2. Overall, all the models performed consistently in collections 2 and 3. The F1-score evaluation results for each test case of all the models demonstrate the applicability of the HR-GLDD training dataset for landslide detection results, especially with employing only the optical bands. The F1-score for HR-GLDD test dataset (collection 1) across all the models was around 72%, which is relatively uniform. Furthermore, the same was observed in the individual test sites in collection 2. We also notice that the Recall and Precision are pretty well balanced ranging between 72.15%-76.61% and 68.13%-75.47%, respectively, indicating stable model predictions (see figure 7). In collection 3, the metrics reveal positive outcomes in terms of mapping the landslides following the event, with an average F1-score of 80% for Haiti and 86% for Indonesia. The recall values are higher than precision values for all the models which have a difference of about 3.32% resulting in F1-score of 72.54% (see figure

395 7). Higher values of recall in all models means that the models were able to identify landslide
396 labelled pixels. However due to the use of only the optical bands, the spectral signatures of
397 other similar features (such as river beds and flat barren areas) were labelled as landslides
398 which result in false predictions, thereby, accounting for lower precision.

399 In figure 8 we chose a single image patch to showcase the predictions of the various models
400 in respect to the referenced ground truth. Despite the differences in the spectral fingerprints
401 of the satellite images for each study site and the events initiated by an earthquake or rainfall,
402 the models were still capable of recognizing landslide features (see figure 9 and 10).

413 Table 2: F1 scores of different DL models across sites and HR-GLDD test dataset along
414 with two unseen test sites.

	Study sites	U-NET	Res-U-NET	Attn-U-NET	Attn-res-Unet	ADSMS-U-NET
	Collection 1 (HR-GLDD Test)	**70.52**	**72.54**	**72.33**	**72.52**	**72.18**
Collection 2	India	75.89	77.77	76.62	77.15	74.21
	Brazil	64.88	71.73	66.19	67.18	64.94
	Nepal	82.65	84.56	81.99	83.15	81.78
	Japan	76.19	76.78	77.5	76.71	77.53
	China2017	60.46	60.13	61.04	60.98	62.37
	China2018	75.04	75.33	75.97	74.44	74.62
	China2019	67.9	70.62	69.93	73.17	70.26
	Myanmar	74.49	76.67	75.96	75.7	74.59
	Collection 3					
	Indonesia	**88.4**	**87.86**	**87.75**	**85.96**	**85.94**
	Haiti	**81.93**	**82.86**	**80.28**	**81.61**	**82.34**

415

416

417
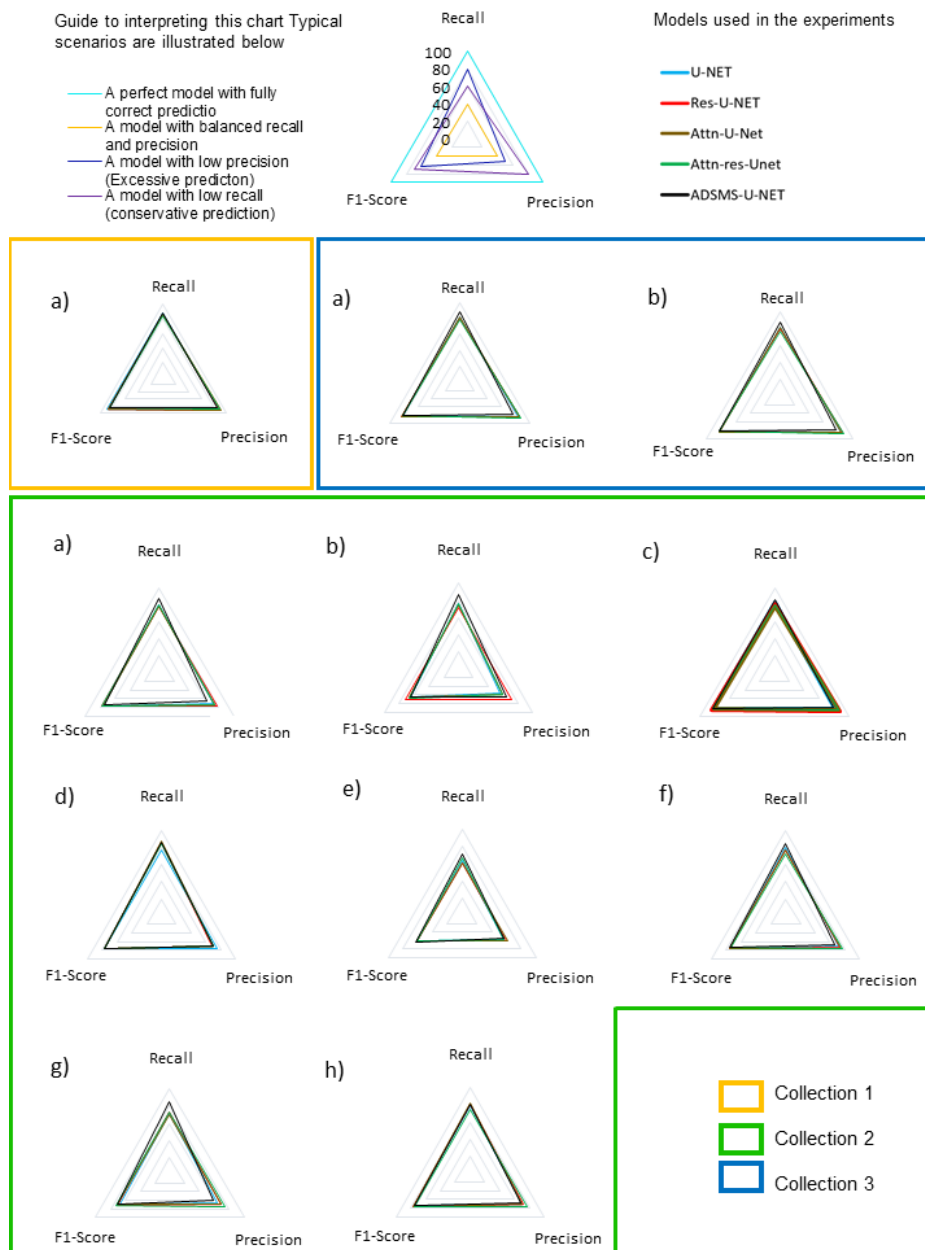
Figure 7: Radar charts visualising the quantitative performance metrics for the DL models
on the three test set collections.

418
419

420

421
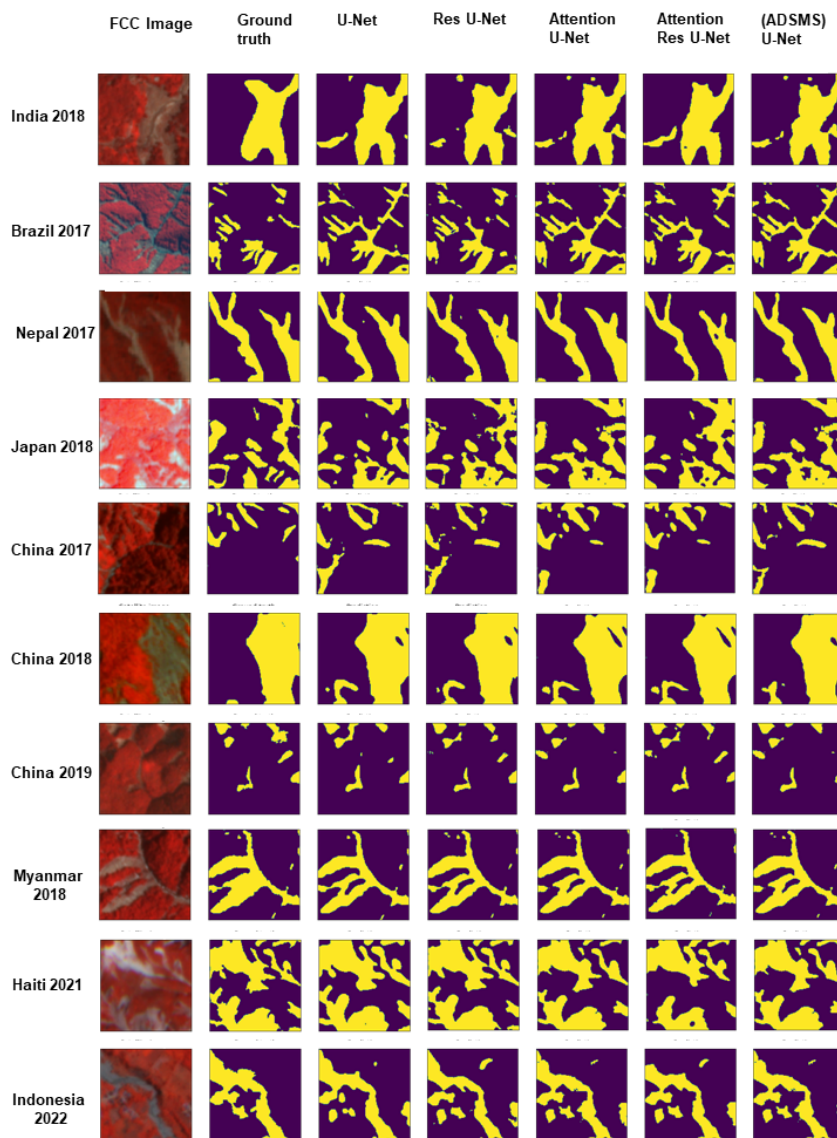
Figure 8: Landslide predictions made by the different DL models against the ground truth. The
base image is shown as a false colour composite (FCC).

424
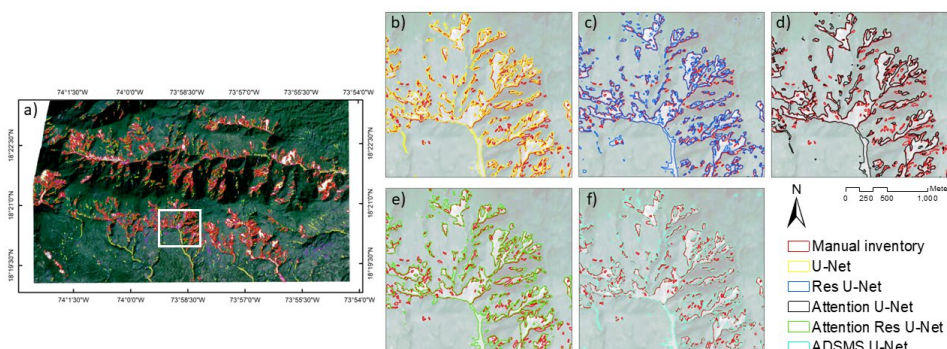
Figure 9: Comparison of ground truth landslides with predictions from the DL models for the
unseen dataset of Haiti.

427
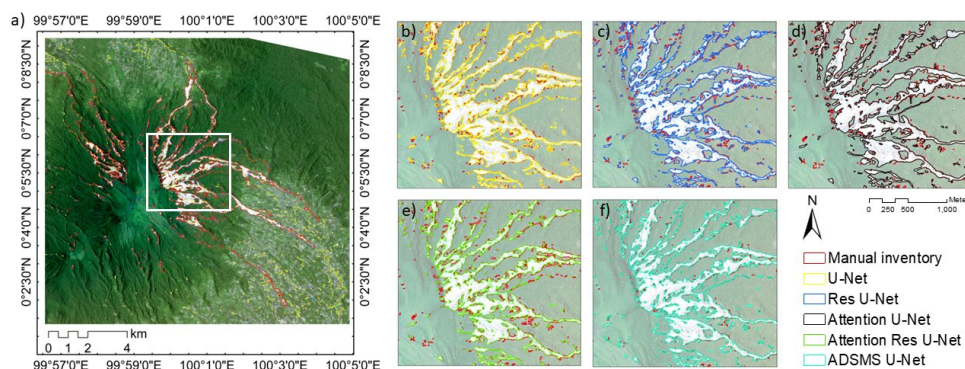
Figure 10: Comparison of ground truth landslides with predictions from the DL models for the
unseen dataset of Indonesia.

6. Discussions

6.1. Advantages of using HR images

The spatial resolution of Planet Scope imagery enables the detection of small size landslides
that open access satellite missions like Sentinel and Landsat frequently miss due to their
spatial and temporal resolution (Meena et al., 2021b). Moreover, even though Sentinel-2 has
additional spectral bands, the lack of improved spatial resolution inhibits precise boundary
delineation and landslide localisation (Meena et al., 2022d). The most prominent features of
Planet Scope imagery, in addition to its competitive spatial resolution, are its daily temporal
resolution and global coverage. Since the satellites have identical sensors, the imagery
are orthorectified and image pre-processing are simplified and more accurate. Because
Planet imagery provide global coverage, we may extend our study sites to new locations for
generating more quality datasets that allow for a better model generalization.

6.2. Quality of HR-GLDD

The quality of any ML/DL model depends on the data that it is trained on, and the GLDD aims
to meet this fundamental requirement. To our knowledge, no other quality data sets exist that
can accommodate the wide range of landslide-triggering events and topographical diversity

448 needed for efficient model training. As the GLDD is a strong collection of various landslide
449 events caused both by rainfall and earthquakes. The GLDD is designed to calibrate models
450 able to map new events that will occur in the future. The models investigated in our study gave
451 promising and consistent results for two unseen datasets generated by completely different
452 events, indicating a well-prepared, dependable, and resilient dataset. However, there are clear
453 limitations with the GLDD that must be considered. These problems primarily stem from issues
454 with manually delineated polygons and various uncertainties caused by satellite imagery. A
455 number of different variables, including the mapping scale, the date, and the quality of the
456 satellite imagery, affect how accurate an inventory is. The radiometric resolution and cloud
457 coverage are additional variables that affect the generation of manual inventories. Additionally,
458 haze effect caused by instrument errors hinders model performances. Subjectivity in the
459 landslide polygon boundaries results from the amalgamation problem, which is caused by
460 elements like the investigators' level of experience and the goal of the study.

461 6.3. Significance of the HR-GLDD

462 A thorough hazard and risk framework is made possible by quality landslide inventories
463 however, the generating such inventories at large scales takes ample amount of time and
464 resources. This is where such automatic pipelines can truly shine at creating inventories which
465 can be used for the successive phases of a hazard and risk. Local, regional, and national
466 stakeholders may include such inventories into their risk reduction efforts thanks to the
467 availability of inventories produced automatically. Furthermore, this information may serve as
468 the foundation for a legal framework that implements landslide risk. A landslide risk reduction
469 plan is now more crucial than ever given the anticipated rise in worldwide landslide activity
470 brought on by climate change. Higher landslide activity is expected in the future due to a
471 number of factors, including an increase in the frequency and intensity of seismic events,
472 anthropogenic events, heavy precipitation events, rising ground water levels, storm surges,
473 and a general rise in relative sea level. Therefore, it is essential to comprehend the underlying
474 mechanisms of landslides better and create practical risk reduction techniques to save
475 people's lives and property.

476 6.4. Automated pipeline for HR-GLDD

477 At the moment, automated techniques are the only viable solution for mapping vast regions
478 with accuracy appropriate for operational objectives. Nonetheless, reliable, reproducible, and
479 accurate processes for automating landslide detection across huge data stacks are still
480 absent. As a result, many landslide-affected regions remain unmapped because 1) they are
481 challenging to map using standard methods, and 2) using high-resolution imagery is costly
482 and labour-intensive, with a substantial part of the mapping process dependent on human
483 judgment. By overcoming these challenges, automated pipelines that address these issues
484 can considerably reduce the requirement for human involvement and pave the way for the
485 development of reliable real-time mapping and monitoring of natural hazards at the continental
486 and global scales. Based on the quality of GLDD, reliability of automated pipelines and rapidly
487 growing availability of HR satellite imagery, we can realistically envision mapping of landslide
488 instances and contribute towards generating and updating landslide inventories at large-
489 scales, spatially and potentially, also temporally (Bhuyan et al., 2022).

490 Providing an expert-based, high-quality, and scientifically validated landslide inventory to
491 scientific communities is essential for frameworks of modelling, landslide prediction, machine
492 learning, and deep learning research. The GLDD dataset has been verified, which increases
493 the availability of much-needed training datasets for automated mapping algorithms. The
494 consistently long time taken to compile landslide inventories manually contrasts with the rise
495 in data accessible for landslide mapping. The development of technologies to successfully

496   automate the procedure is the future direction in landslide inventory mapping. The precedence
497   of quality dataset is noted in where they commented that the need for quality datasets will
498   provide a valuable resource for training and developing algorithms.

499   The current dataset is an excellent resource for training and developing future algorithms for
500   this purpose. Automated mapping methods, particularly when combined with publicly available
501   elevation models, can potentially improve our results in future investigations.

502   7. Conclusions

503   Mapping landslides through space is a challenging endeavour. Automated efforts for the same
504   have been explored to some extent, but a transferrable method based on a robust dataset has
505   not yet been investigated. In this paper, we propose a reliable dataset which can be employed
506   by deep learning algorithms to detect new landslides accurately. The predictive capabilities
507   demonstrate the usefulness and application of the dataset to map landslides at large scales.
508   However, the model's predictability must be investigated further in order to identify particular
509   problems to enhance the findings and predictive capabilities for more complicated landscapes.
510   Overall, despite the limitations, the findings are promising, since it is the first time such a HR
511   dataset has been created that caters to a transferable approach of mapping landslides at so
512   many different geomorphological and geographical locations.

513   Data availability

514   The data, working codes and a document with metadata are freely available at
515   https://github.com/kushanavbhuyan/HR-GLDD-A-Global-Landslide-Mapping-Data-
516   Repository where data in the format of arrays and model configurations in the framework of
517   TensorFlow as can be displayed and used for reproducibility of our results. We also submit
518   the generated landslide inventories in the form of an Environmental Systems Research
519   Institute (ESRI) shapefile. Modules for deep learning can be found at
520   https://www.tensorflow.org/ and original satellite imageries can be found at
521   https://www.planet.com/.

522   Code availability

523   Code used to produce data described in this manuscript, as well as to create figures and
524   tables, can be accessed at https://github.com/kushanavbhuyan/HR-GLDD-A-Global-
525   Landslide-Mapping-Data-Repository

526   Author contribution

527   All the authors contributed to equally to preparation of manuscript from data curation to review
528   of final manuscript.

529   Competing interests The authors declare that they have no conflict of interest.

530   **References**

531   Abderrahim, N. Y. Q., Abderrahim, S., & Rida, A. (2020). Road Segmentation using U-Net
532   architecture. *2020 IEEE International Conference of Moroccan Geomatics (Morgeo)*, 1–4.
533   https://doi.org/10.1109/Morgeo49228.2020.9121887

534   Abraham, N., & Mefraz Khan, N. (2018). *A NOVEL FOCAL TVERSKY LOSS FUNCTION*
535   *WITH IMPROVED ATTENTION U-NET FOR LESION SEGMENTATION.*
536   https://github.com/nabsabraham/focal-tversky-unet

537 Alpert, L. (1942). Rainfall map of Hispaniola. *Bulletin of the American Meteorological Society*,
538 *23*, 423–431.

539 Amatya, P., Kirschbaum, D., & Stanley, T. (2022). Rainfall-induced landslide inventories for
540 Lower Mekong based on Planet imagery and semi-automatic mapping method. *Geoscience*
541 *Data Journal*, *00*, 1–13. https://doi.org/10.1002/gdj3.145

542 Bai, H., Feng, W., Yi, X., Fang, H., Wu, Y., Deng, P., Dai, H., & Hu, R. (2021). Group-occurring
543 landslides and debris flows caused by the continuous heavy rainfall in June 2019 in Mibei
544 Village, Longchuan County, Guangdong Province, China. *Natural Hazards*, *108*(3), 3181–
545 3201. https://doi.org/10.1007/s11069-021-04819-1

546 Bhuyan, K., Meena, S. R., Nava, L., van Westen, C. J., Floris, M., & Catani, F. (2022). Mapping
547 landslides through a temporal lens: An insight towards multi-temporal landslide mapping using
548 the U-Net deep learning model. *Earth Arxiv*. https://doi.org/https://doi.org/10.31223/X5DM0B

549 Cruden, D. M., & Varnes, D. (1996). LANDSLIDE TYPES AND PROCESSES. In *National*
550 *Research Council, Transportation Research Board*.

551 Diakogiannis, F. I., Waldner, F., Caccetta, P., & Wu, C. (2020). ResUNet-a: A deep learning
552 framework for semantic segmentation of remotely sensed data. *ISPRS Journal of*
553 *Photogrammetry and Remote Sensing*, *162*, 94–114.
554 https://doi.org/10.1016/j.isprsjprs.2020.01.013

555 EM-DAT. (2018). *The emergency events database—Universit´ e catholique de Louvain*
556 *(UCL)—CRED, D Guha-Sapir*.

557 Fadhilah, & Prabowo, H. (2020). Genes and physical properties of iron sand from Kinali
558 Pasaman. *Journal of Physics: Conference Series*, *1481*(1). https://doi.org/10.1088/1742-
559 6596/1481/1/012015

560 Fan, X., Scaringi, G., Domènech, G., Yang, F., Guo, X., Dai, L., He, C., Xu, Q., & Huang, R.
561 (2019). Two multi-temporal datasets that track the enhanced landsliding after the 2008
562 Wenchuan earthquake. *Earth System Science Data*, *11*(1), 35–55.
563 https://doi.org/10.5194/essd-11-35-2019

564 Feng, W., Bai, H., Lan, B., Wu, Y., Wu, Z., Yan, L., & Ma, X. (2022). Spatial–temporal
565 distribution and failure mechanism of group-occurring landslides in Mibei village, Longchuan
566 County, Guangdong, China. *Landslides*, *May*. https://doi.org/10.1007/s10346-022-01904-9

567 Fred Agarap, A. M. (n.d.). *Deep Learning using Rectified Linear Units (ReLU)*. Retrieved
568 August 15, 2022, from https://github.com/AFAgarap/relu-classifier.

569 Froude, M. J., & Petley, D. N. (2018). Global fatal landslide occurrence from 2004 to 2016.
570 *Natural Hazards and Earth System Sciences*, *18*(8), 2161–2181.
571 https://doi.org/10.5194/nhess-18-2161-2018

572 Ghorbanzadeh, O., Xu, Y., Ghamisi, P., Kopp, M., & Kreil, D. (2022). *Landslide4Sense:*
573 *Reference Benchmark Data and Deep Learning Models for Landslide Detection*.
574 https://doi.org/10.48550/arxiv.2206.00515

575 Harp, E. L., Jibson, R. W., & Schmitt, R. G. (2016). *Map of landslides triggered by the January*
576 *12, 2010, Haiti earthquake*. https://doi.org/10.3133/sim3353

577 Hungr, O., Leroueil, S., & Picarelli, L. (2014). The Varnes classification of landslide types, an
578 update. In *Landslides* (Vol. 11, Issue 2, pp. 167–194). Springer Verlag.
579 https://doi.org/10.1007/s10346-013-0436-y

580 Jain, A. K., & Banerjee, D. M. (2020). The Indian Subcontinent: Its tectonics. In *Proceedings*
581 *of the Indian National Science Academy* (Vol. 86, Issue 1).
582 https://doi.org/10.16943/ptinsa/2020/49834

583 Karki, R., Talchabhadel, R., Aalto, J., & Baidya, S. K. (2016). New climatic classification of
584 Nepal. *Theoretical and Applied Climatology*, *125*(3–4), 799–808.
585 https://doi.org/10.1007/s00704-015-1549-0

586 Kingma, D. P., & Lei Ba, J. (n.d.). *ADAM: A METHOD FOR STOCHASTIC OPTIMIZATION*.

587 Lee, C.-Y., Xie, S., Gallagher, P., Zhang, Z., & Tu, Z. (n.d.). *Deeply-Supervised Nets*.

588 Liu, Y. ;, Yao, X. ;, Gu, Z. ;, Zhou, Z. ;, Liu, X. ;, Chen, X. ;, Wei, S., Liu, Y., Yao, X., Gu, Z.,
589 Zhou, Z., Liu, X., Chen, X., & Wei, S. (2022). Study of the Automatic Recognition of Landslides
590 by Using InSAR Images and the Improved Mask R-CNN Model in the Eastern Tibet Plateau.
591 *Remote Sensing 2022, Vol. 14, Page 3362*, *14*(14), 3362.
592 https://doi.org/10.3390/RS14143362

593 Martinez, S. N., Allstadt, K. E., Slaughter, S. L., Schmitt, R. G., Collins, E., Schaefer, L. N., &
594 Ellison, S. (2021). Landslides triggered by the August 14, 2021, magnitude 7.2 Nippes, Haiti,
595 earthquake. *Open-File Report*.

596 Meena, S. R., Ghorbanzadeh, O., van Westen, C. J., Nachappa, T. G., Blaschke, T., Singh,
597 R. P., & Sarkar, R. (2021a). Rapid mapping of landslides in the Western Ghats (India) triggered
598 by 2018 extreme monsoon rainfall using a deep learning approach. *LANDSLIDES*, *18*(5),
599 1937–1950. https://doi.org/10.1007/s10346-020-01602-4

600 Meena, S. R., Ghorbanzadeh, O., van Westen, C. J., Nachappa, T. G., Blaschke, T.,
601 Singh, R. P., & Sarkar, R. (2021b). Rapid mapping of landslides in the Western Ghats
602 (India) triggered by 2018 extreme monsoon rainfall using a deep learning approach.
603 *Landslides*, *18*(5). https://doi.org/10.1007/s10346-020-01602-4

604 Meena, S. R., Soares, L. P., Grohmann, C. H., van Westen, C., Bhuyan, K., Singh, R. P.,
605 Floris, M., & Catani, F. (2022a). Landslide detection in the Himalayas using machine learning
606 algorithms and U-Net. *Landslides*. https://doi.org/10.1007/s10346-022-01861-3

607 Meena, S. R., Soares, L. P., Grohmann, C. H., van Westen, C., Bhuyan, K., Singh, R. P.,
608 Floris, M., & Catani, F. (2022b). Landslide detection in the Himalayas using machine learning
609 algorithms and U-Net. *Landslides*, *19*(5), 1209–1229. https://doi.org/10.1007/s10346-022-
610 01861-3

611 Meena, S. R., Soares, L. P., Grohmann, C. H., van Westen, C., Bhuyan, K., Singh, R. P.,
612 Floris, M., & Catani, F. (2022c). Landslide detection in the Himalayas using machine
613 learning algorithms and U-Net. *Landslides*, *19*(5), 1209–1229.
614 https://doi.org/10.1007/s10346-022-01861-3

615 Meena, S. R., Soares, L. P., Grohmann, C. H., van Westen, C., Bhuyan, K., Singh, R. P.,
616 Floris, M., & Catani, F. (2022d). Landslide detection in the Himalayas using machine learning
617 algorithms and U-Net. *LANDSLIDES*, *19*(5), 1209–1229. https://doi.org/10.1007/s10346-022-
618 01861-3

619 Meena, S. R., Soares, L. P., Grohmann, C. H., van Westen, C., Bhuyan, K., Singh, R. P.,
620 Floris, M., & Catani, F. (2022e). Landslide detection in the Himalayas using machine learning
621 algorithms and U-Net. *Landslides*, *19*(5), 1209–1229. https://doi.org/10.1007/S10346-022-
622 01861-3/FIGURES/10

623 Milletari, F., Navab, N., & Ahmadi, S.-A. (n.d.). *V-Net: Fully Convolutional Neural Networks for*
624 *Volumetric Medical Image Segmentation*. http://promise12.grand-challenge.org/results/

625 Nava, L., Bhuyan, K., Meena, S. R., Monserrat, O., & Catani, F. (2022). Rapid Mapping of
626 Landslides on SAR Data by Attention U-Net. *Remote Sensing 2022, Vol. 14, Page 1449*, *14*(6),
627 1449. https://doi.org/10.3390/RS14061449

628 Nava, L., Monserrat, O., & Catani, F. (2022). Improving Landslide Detection on SAR Data
629 Through Deep Learning. *IEEE Geoscience and Remote Sensing Letters*, *19*.
630 https://doi.org/10.1109/LGRS.2021.3127073

631 Oktay, O., Schlemper, J., le Folgoc, L., Lee, M., Heinrich, M., Misawa, K., Mori, K., Mcdonagh,
632 S., Hammerla, N. Y., Kainz, B., Glocker, B., & Rueckert, D. (n.d.). *Attention U-Net: Learning*
633 *Where to Look for the Pancreas*.

634 Planet Team. (2019). *Planet Imagery Product Specifications August 2019*. 97.

635 Prakash, N., Manconi, A., & Loew, S. (2021). A new strategy to map landslides with a
636 generalized convolutional neural network. *Scientific Reports*, *11*(1), 1–15.
637 https://doi.org/10.1038/s41598-021-89015-8

638 Roback, K., Clark, M. K., West, A. J., Zekkos, D., Li, G., Gallen, S. F., Chamlagain, D., & Godt,
639 J. W. (2018). The size, distribution, and mobility of landslides caused by the 2015 Mw7.8
640 Gorkha earthquake, Nepal. *Geomorphology*, *301*, 121–138.
641 https://doi.org/10.1016/j.geomorph.2017.01.030

642 Ronneberger, O., Fischer, P., & Brox, T. (2015). *U-Net: Convolutional Networks for Biomedical*
643 *Image Segmentation* (pp. 234–241). https://doi.org/10.1007/978-3-319-24574-4_28

644 Soares, L. P., Dias, H. C., Garcia, G. P. B., & Grohmann, C. H. (2022a). Landslide
645 Segmentation with Deep Learning: Evaluating Model Generalization in Rainfall-Induced
646 Landslides in Brazil. *Remote Sensing*, *14*(9), 2237. https://doi.org/10.3390/rs14092237

647 Soares, L. P., Dias, H. C., Garcia, G. P. B., & Grohmann, C. H. (2022b). Landslide
648 Segmentation with Deep Learning: Evaluating Model Generalization in Rainfall-Induced
649 Landslides in Brazil. *Remote Sensing*, *14*(9), 2237. https://doi.org/10.3390/rs14092237

650 Tang, X., Tu, Z., Wang, Y., Liu, M., Li, D., & Fan, X. (2022). Automatic Detection of Coseismic
651 Landslides Using a New Transformer Method. *Remote Sensing*, *14*(12), 2884.
652 https://doi.org/10.3390/rs14122884

653 Tiwari, B., Ajmera, B., & Dhital, S. (2017). Characteristics of moderate- to large-scale
654 landslides triggered by the Mw 7.8 2015 Gorkha earthquake and its aftershocks. *Landslides*,
655 *14*(4), 1297–1318. https://doi.org/10.1007/s10346-016-0789-0

656 USAID. (2014). *Haiti Securite Alimentaire en Bref*.

657 Wang, F., Fan, X., Yunus, A. P., Siva Subramanian, S., Alonso-Rodriguez, A., Dai, L., Xu, Q.,
658 & Huang, R. (2019). Coseismic landslides triggered by the 2018 Hokkaido, Japan (Mw 6.6),
659 earthquake: spatial distribution, controlling factors, and possible failure mechanism.
660 *Landslides*, *16*(8), 1551–1566. https://doi.org/10.1007/s10346-019-01187-7

661 Wilis, R. (2019). Impact Variability of Rainfall Intensity to Horticulture Productivity at West
662 Pasaman Regency , Province of West Sumatera , Indonesia. *Core.Ac.Uk*, *7*(10), 138–145.

663 Win Zin, W., & Rutten, M. (2017). Long-term Changes in Annual Precipitation and Monsoon
664 Seasonal Characteristics in Myanmar. *Hydrology: Current Research*, *08*(02).
665 https://doi.org/10.4172/2157-7587.1000271

666 Yang, Z., & Xu, C. (2022). Efficient Detection of Earthquake−Triggered Landslides Based on
667 U−Net++: An Example of the 2018 Hokkaido Eastern Iburi (Japan) Mw = 6.6 Earthquake.
668 *Remote Sensing*, *14*(12), 2826. https://doi.org/10.3390/rs14122826

669 Yang, Z., Xu, C., & Li, L. (2022). Landslide Detection Based on ResU-Net with Transformer
670 and CBAM Embedded: Two Examples with Geologically Different Environments. *Remote*
671 *Sensing*, *14*(12), 2885. https://doi.org/10.3390/rs14122885

672 Zulkarnain, I. (2016). Sumatra is not a homogeneous segment of Gondwana derived continel
673 blocks: A New Sight based on Geochemical Signatures of Pasaman Volcanic in West
674 Sumatera. *Jurnal RISET Geologi Dan Pertambangan*, *26*(1), 1.
675 https://doi.org/10.14203/risetgeotam2016.v26.271

676

677